43rd AIAA Fluid Dynamics Conference, June 24-27, 2013, San Diego, California

Roughness Induced Transition in a Supersonic Boundary Layer

P. Balakumar and Michael Kegerise
Flow Physics and Control Branch
NASA Langley Research Center, Hampton, VA 23681

Direct numerical simulation is used to investigate the transition induced by three-dimensional isolated roughness elements in a supersonic boundary layer at a free stream Mach number of 3.5. Simulations are performed for two different configurations: one is a square planform roughness and the other is a diamond planform roughness. The mean-flow calculations show that the roughness induces counter rotating streamwise vortices downstream of the roughness. These vortices persist for a long distance downstream and lift the low momentum fluid from the near wall region and place it near the outer part of the boundary layer. This forms highly inflectional boundary layer profiles. These observations agree with recent experimental observations. The receptivity calculations showed that the amplitudes of the mass-flux fluctuations near the neutral point for the diamond shape roughness are the same as the amplitude of the acoustic disturbances. They are three times smaller for the square shape roughness.

I. Introduction

Surface roughness is known to enhance the laminar-to-turbulent transition process in both low- and high-speed boundary layers. As such, predicting whether the flow over a given roughness distribution will remain laminar or become turbulent is an important concern. The parameter space associated with roughness-induced transition is very broad and includes factors such as: (1) roughness type (isolated versus distributed); (2) roughness height and shape (two- or three-dimensional); (3) flow parameters such as Mach number and Reynolds number; and (4) freestream disturbance levels. Generally, we categorize the effects of roughness into three groups based on the relative roughness height, k/δ, where k is roughness height and δ is the boundary layer thickness: (1) small roughness ($k/\delta << 1$); (2) medium roughness ($k/\delta \sim ½$); and (3) large roughness ($k/\delta \sim 1$). In this paper, we focus on the effects of medium height three dimensional roughness elements on the stability and transition of supersonic laminar boundary layers.

Boundary-layer transition in quiet environments with small roughness elements occurs due to exponential growth of linear instability waves.[1] In subsonic flows, the unstable waves are the low frequency, long wavelength two-dimensional Tollmien-Schlichting (T-S) waves. These waves are generated by freestream acoustic disturbances and/or by the interaction of freestream acoustic disturbances with small isolated or distributed roughness elements.[2,3] Small roughness elements introduce localized steady perturbations to the boundary layer. The freestream unsteady disturbances interact with these steady perturbations and generate the instability waves inside the boundary layer. In supersonic flows, unstable disturbances are high frequency three-dimensional waves with phase speeds approximately equivalent to that of the acoustic waves. Hence, these disturbances are efficiently generated by the freestream acoustic disturbances.[4,5] In hypersonic boundary layers, unstable waves are very high frequency two-dimensional waves with phase speeds equivalent also to the acoustic waves. Hence, these waves are also efficiently generated by the freestream acoustic disturbances.[4,6,7] In supersonic and hypersonic boundary layers, the critical layers are situated in the outer part of the boundary layer and so small roughness elements have minimal influence on the receptivity or on the stability of the boundary layer. Our recent investigation[8] on the effects of isolated and distributed two-dimensional roughness elements on the stability of a hypersonic boundary layer at a free stream of Mach number of 6 revealed that distributed small roughness elements located across the continuous spectrum increased the receptivity of the second mode generated by the slow and fast acoustic waves and the vorticity wave by about 4.6, 4.5 and 11.8 times, respectively.

With increasing roughness heights, the modified mean flow in the roughness wake becomes more inflectional and unstable compared to the unmodified boundary layer. Klebanoff *et al.*[9,10] performed detailed

experimental investigations of the mechanisms involved in two- and three-dimensional roughness-induced transition in incompressible flows. The major findings are that two-dimensional roughness elements cause early transition compared to that without roughness due to the destabilizing influence of the inflectional boundary layer profiles behind the roughness. It was also demonstrated that the upstream movement of the transition point towards the roughness is gradual with increasing Reynolds number. One important finding in the transition induced by a three-dimensional roughness element is that after a critical Reynolds number, the transition front moves rapidly towards the roughness element with a small increase in Reynolds number. The critical roughness Reynolds number for a hemispherical roughness was $Re_k = U_k\, k / \nu = 325$. The critical Reynolds number was 450 for a cylindrical element. Here, U_k is the velocity of the unperturbed boundary layer at the roughness height k. Detailed hot-wire measurements in the vicinity of the roughness element showed the existence of well defined periodic disturbances downstream of the roughness element. It was postulated that the flow field immediately behind the roughness consists of waves and these waves change to hairpin vortices downstream. With increasing velocity, the shedding of hairpin vortices starts immediately downstream of the roughness. These observations agree with the flow visualization studies of Acarlar and Smith.[11] Flow visualization studies by Gregory and Walker[12] showed the appearance of two streaks in the roughness wake, spaced at one roughness diameter apart. As the roughness height was increased, a turbulent wedge formed downstream and gradually moved towards the roughness. Large roughness heights showed the appearance of a horseshoe vortex wrapped around the roughness and trailing downstream parallel to the direction of the flow. Smoke visualizations performed at Reynolds numbers below the critical value revealed a pair of spiral smoke filaments behind the cylinder, trailing downstream along the centerline.

Until recently, most of the previous high-speed roughness-induced transition investigations were wind tunnel and flight experiments concentrating on developing correlation data or functions relating the transition Reynolds number with some roughness parameters. Recent review papers by Reda[13] and Schneider[14,15] provide a detailed summary of roughness-induced transition in high-speed flows and different correlation expressions used in applications. Schneider[14] summarized the effects of roughness shape, Mach number and wall temperature on roughness-induced transition. An interesting and well-known fact is the sharp increase of the effective roughness Reynolds number with increasing Mach number. The effective roughness Reynolds number is about 200 at a freestream Mach number of 3 and it increases to about 2000 at a freestream Mach number of 6. The effective roughness Reynolds number is defined as the minimum roughness Reynolds number at which the transition from laminar to turbulent occurs very close to the roughness. The state of the art prediction method is to use some correlation expression that depends on the roughness parameters and flow conditions calibrated from experiments. Typically, these correlations yield a critical roughness Reynolds number that is based on the roughness height and the flow conditions at the roughness height. This gives reasonable predictions[16] provided the correlation expressions are used under conditions and environments similar to those for which the correlations were derived.

With recent advances in computational and experimental techniques, attempts have been made[17-25] to understand the transition process behind an isolated roughness element and hence to predict the transition onset behind the roughness based on these physical processes. Flow visualization[17] using Nitric Oxide Planar Laser-Induced Fluorescence (NO-PLIF) technique of flow structures induced by hemispherical roughness was performed in the NASA Langley Research Center Mach 10 wind tunnel. The images showed the streamwise vortices behind the roughness and the breakdown of these vortices to turbulence downstream of the roughness. Detailed mean-flow and fluctuating measurements with pitot and hot-wire probes were performed in the wake of a large roughness element ($k/\delta = 1.1$) located on the nozzle wall of the Boeing/AFOSR Mach 6 Quiet Tunnel.[18] There, a flow instability near 21 kHz was detected behind the roughness. Simulations of this experiment by Bartkowicz *et al*.[19] also observed oscillations at this frequency, both upstream and downstream of the roughness. Computations also revealed that the origin of this instability is the unstable vortex-shock system that exists upstream of the cylindrical roughness.

Computations[20] of the flow behind an isolated roughness element with $k/\delta \sim 0.5$ in a supersonic boundary layer at a freestream Mach number of 3.5 showed that the wake behind the roughness consists of a low-speed streak along the symmetry plane surrounded by two high-speed streaks on either side. It was also observed that this wake structure is steady and persists over a long distance downstream. Associated with these low- and high-speed streaks is the formation of thick highly inflectional boundary layers along the symmetry plane and strong inflectional profiles in the spanwise direction. A two-dimensional stability analysis of the wake revealed two families of instability modes: (1) even or symmetric modes; and (2) odd or anti-symmetric modes. The even modes are associated with the wall normal shear and the odd modes are associated with the spanwise shear. Simulations[21] performed at a higher freestream Mach number of 5.9 also revealed similar flow and instability

structure behind the roughness. Computations[23,24] performed at a free stream Mach number of 4.8 also revealed the same streaky wake structure and similar instability characteristics.

Recently, a detailed roughness experiment[25] was performed in the NASA Langley Research Center Low-Disturbance-Supersonic-Tunnel (SLDT) at a free stream Mach number of 3.5. A three-dimensional diamond shape roughness element with k/δ = 0.48 was placed on a flat plate at a short distance from the leading edge. The mean flow field and the unsteady mass-flux fluctuations in the wake of the roughness were mapped out using pitot and hot-wire probes. The measurements agreed very well with the computational results. The power spectral density (PSD) showed dominant high-frequency disturbances in the wake of the roughness, and these disturbances grow in amplitude with increasing streamwise direction and subsequently breakdown to turbulence farther downstream.

In this paper we simulate the experiment of Kegerise *et al.*[25] using Direct Numerical Simulations (DNS). The objectives are to answer (1) how do isolated finite height roughness elements modify the incoming boundary layer, (2) how do external acoustic disturbances generate the wake instability waves, and (3) how do the instability waves evolve downstream. The approach is to first solve for the mean flow with the roughness elements of square and diamond planform shapes. The second step is to superimpose two- and three-dimensional acoustic disturbances on the freestream and to perform time-accurate simulations to investigate the generation and evolution of disturbances in the wake. We use the same parameters that were used in the experiment.

II. Models and Flow Conditions

Computations are performed for a supersonic flow over a flat plate with a blunt leading edge. The leading edge thickness is 0.00125 inches. The schematic diagram of the computational setup is depicted in Fig. 1. The Cartesian axes (x, y, z) are aligned in the streamwise, normal and spanwise direction respectively. The flow conditions are the same as in the experiments of Kegerise *et al.*[25] The freestream Mach number is 3.5 and the freestream stagnation temperature is 319 K. The experiments were performed at two unit Reynolds numbers of 10.8 and $9.0*10^6$/m, corresponding to stagnation pressures of 206.8 and 172.4 kPa. The simulations were performed for a constant wall temperature of 290 K. The Sutherland viscosity law was used with a constant Prandtl number of 0.70.

A. Isolated Roughness

The three-dimensional cubic roughness element is of the form:

$$y_c(x) = \frac{k}{2}\left[\tanh\sigma_x \frac{x-(x_0-l/2)}{\Delta x} - \tanh\sigma_x \frac{x+(x_0+l/2)}{\Delta x}\right] \tag{1}$$

$$y_{3d}(x,z) = y_c(x)\left[\tanh\sigma_z \frac{z-z_0}{\Delta z} - \tanh\sigma_z \frac{z+z_0}{\Delta z}\right]. \tag{2}$$

Here $y_{3d}(x, z)$ is the height of the roughness normal to the surface of the plate, k is the maximum height, x_o is the location of the center of the roughness, l is the width of the roughness, and σ_x and Δx determine the streamwise spatial extent of the roughness near the edges. The parameter, z_o, is the starting location of the roughness in the spanwise direction, and σ_z and Δz determine the spanwise extent of the roughness near the edges. The location of the roughness and the dimensions of the roughness are the same as in the experiments[25]. The planform of the roughness is a square shape with length of 2.54 mm, while the height of the roughness is 0.345 mm. The center of the roughness is located at x = 41.5 mm from the leading edge of the plate. In the experiment, only the diamond planform roughness (configuration 1 in Fig. 1b) was considered. To evaluate the effect of different orientations of the roughness on the transition, simulations are also performed with the square planform roughness (configuration 2 in Fig. 1c). Hence in the diamond shape planform, the roughness spans to $l\sqrt{2} = 3.59$ mm in the spanwise and in the axial directions. The leading edge and trailing edge of the roughness are located at 40.23 and 42.77 mm for the square planform and are located at 39.70 and 43.30 mm for the diamond planform. The spanwise extents are z = ±1.27 and 1.80 mm for the square and diamond form respectively.

III. Numerical method

A. Solution Algorithm

The three-dimensional unsteady compressible Navier-Stokes equations, written in conservation form were solved using a 5th-order accurate weighted essentially non-oscillatory (WENO) scheme for space discretization and a 3rd-order total-variation-diminishing (TVD) Runge-Kutta scheme for time integration. The WENO and TVD methods and formulas are explained in Shu[26]. The application of the ENO method to the Navier-Stokes equations is presented in Atkins[27]. The solution method implemented in the present computations is described in Balakumar *et al*.[5]

We used a body-fitted curvilinear grid system in all of the simulations. The grid stretches in the wall normal η direction close to the wall and is uniform outside the boundary layer. In the streamwise ξ direction, the grid is symmetric about and very fine near the leading edge, and subsequently becomes uniform in the flat region of the plate surface. The grid is uniform in the spanwise ζ direction. The boundary outside of the shock follows a parabola where the vertex is located a short distance upstream of the leading edge to capture the boundary layer accurately. The computational domain extends from x = -0.10 mm to 200 mm in the x direction, and three times the half width of the roughness in the z direction. Figures 2(a-b) show the grid system employed for the flow over a three-dimensional roughness element. Figure 2a depicts the grid distribution in one (x, y) plane for z = 0 while Fig. 2b shows the body-fitted grid over the roughness in one (y, z) plane across the roughness. We used 251 points in the normal direction, 129 points in the spanwise direction. The velocity, density, temperature and pressure are non-dimensionalized by the corresponding freestream values.

IV. Results

A. Mean Flow Results

Simulations were performed for both diamond and square planform geometries. First we present the results for the higher unit Reynolds number case and discuss in detail the results for the diamond planform case. Figure 3 shows the mean flow density profiles obtained for a smooth flat plate at a unit Reynolds number of $10.8*10^6$/m. We plotted the boundary layer profiles for the smooth case in the similarity coordinate in Fig. 3b. The boundary layer has not reached the similarity solution at the roughness location. This is due to the small unit Reynolds number. The boundary layer thickness at the roughness location is about 1.0 mm. This yields a ratio of the roughness height to the boundary layer thickness of k/δ = 0.345. The roughness Reynolds number, $Re_{kk} = U_k k/\nu_k$, which is based on undisturbed conditions at the roughness height, was 393. This is slightly lower than that based on the similarity solution of 462. Figure 4 shows the density contours and the streamlines in the symmetry plane, z = 0, over the diamond-shape roughness. The figure shows the compression wave formed in front of the roughness element, an over expansion over the roughness, and the final recompression downstream. The flow also separates upstream and downstream of the roughness in the symmetry plane. It is interesting to see that the reattachment point on the front face of the roughness is located close to the top of the roughness at about $y/k \sim 0.9$. Figure 5(a, b) shows a perspective view of the streamlines over the diamond and square shape roughness elements. We initiated the streamlines along a virtual rake in the spanwise direction at a constant y location. The blue streamlines show the streamlines that are initiated at a constant height of y/k = 0.45 at the axial location of x = 36 mm. As expected these streamlines are diverted by the front of the roughness to the sides. As the streamlines wrap around the roughness, they subsequently trace the horseshoe vortex that rotates inwards and trails along the axial direction with the legs at about one roughness width apart. The red streamlines originate at a height of $y/k \sim 0.7$. These streamlines flow over the top of the roughness and trace a pair of spiral vortices rotating upwards along the central part of the roughness. These observations agree with the Gregory and Walker[12] smoke visualizations of vortices behind a cylindrical roughness at low speed. The flow over the square roughness is qualitatively similar, but the horseshoe vortex system is spaced closer together since the spanwise extent of the square roughness element is smaller.

Figures 6(a-h) depict the mass-flux contours in several cross-sectional planes over and downstream of the diamond-shape roughness. We also included two-dimensional streamline patterns in these figures. The leading edge of the roughness is located at x=39.7 mm and the trailing edge of the roughness is located at x=43.3 mm. Figure 6(c) shows that streamwise vortices start to appear on the side of the roughness and push the high speed fluid towards the wall at the side of the roughness. Farther downstream (Fig. 6d), the uplifting of the low-speed fluid towards the outer boundary layer near the symmetry plane becomes stronger. This is accompanied by high-speed fluid that is pushed towards the wall on both sides of the wake. One centerline spiral vortex and one leg of the horseshoe vortex appear clearly in Figs. 6(e-f). The clockwise rotating center vortex is located at

about z = 0.9 mm and the leg of the horseshoe vortex is located at about z = 2.0 mm. This is equivalent to about 0.25 and 0.56 times the width of the roughness.

Figures 7(a, b) show the streamwise velocity contours across the middle of the boundary layer, $y/\delta \sim 0.4$ in the (x-z) plane for the flow over the diamond and square shapes respectively. It is interesting to observe the appearance of the low-speed streak in the middle of the wake. This streak is surrounded by high-speed streaks on either side of the wake. The figures show that the high-speed streaks originate at the corners of the roughness and move slightly inwards and remain parallel to the x-axis. Another interesting observation is the persistence of these streaks for a long distance downstream.

Figure 8(a) shows the mean mass flux profiles along the symmetry plane at increasing x stations generated by the diamond-shape roughness. We also included the measured mass-flux profiles at two streamwise stations, x = 58.8 and 84.7 mm. The measured velocity profiles are slightly above the computed profiles. In part, this may be due to the different incoming boundary layers between the computations and experiments or it may be due to the smooth edge roughness shape we used in the simulation instead of the sharp-edge shape that exists in the experiment. As we discussed previously, the lift up of the low-speed fluid by the vortex increases the boundary layer thickness and produces profiles that are inflectional in character. This leads to a strong instability of the wake and early breakdown to a turbulent boundary layer. Figure 8(b) shows the mass flux profiles for the square shape roughness case. The experimental results are not available yet. For comparison, we included the computed profiles for the diamond shape at x=58.87, 93.37 and 127.97 mm. The boundary layer profiles are thicker for the diamond shape than that for the square shape. It would be interesting to see whether this will change if we performed the calculation for a square-shape roughness with the same frontal width as the diamond-shape roughness considered here.

Figures 9(a-c) depict the variation of the streamwise velocity, U, in the spanwise direction at x stations of 43.8, 47.0 and 136.5 mm, respectively. These stations correspond to immediately downstream, about 15 and 360 roughness heights downstream. The different lines in each plot show the variation of the velocity at increasing heights in the boundary layer. The first observation is that the velocity distribution behind the roughness resembles the wake profiles behind a two-dimensional cylinder with an over shoot at the edges. There are two inflectional profiles on each side of the roughness. The spanwise velocity gradient of the profiles towards the center is stronger than that towards the outside. Due to the existence of the inflectional profiles in the wall-normal direction (Fig. 8) and in the spanwise direction, the wake structure behind a three-dimensional roughness exhibits several instability modes as shown in the computations[20,21] and in the experiment[25]. Similarly, Figs. 10(a-c) present the streamwise velocity profiles in the spanwise direction for the square-shape roughness.

We also performed the calculations at a smaller unit Reynolds number of $9.0*10^6$/m for the diamond shape roughness with the same roughness parameters. Since the boundary layer is thicker in this case, the roughness Reynolds number is Re_{kk} = 279. Figure 11 shows the mass-flux profiles along the centerline at different axial stations. We also included the experimental results[25] and the computed mass-flux profiles obtained at the higher Reynolds number of $10.8*10^6$/m. Similar to the previous case, Fig. 8, the measured profiles are thicker than that are computed. Interestingly, the boundary layer profiles computed at the two unit Reynolds numbers cases differ only by a small amount, even though the roughness Reynolds numbers are different, 393 and 279, respectively.

B. Interaction of Slow Acoustic Waves with Three-dimensional Isolated Roughness

The next question to answer is how do external acoustic disturbances generate instability waves in the roughness wake. Recent two-dimensional eigenvalue computations[20,21] and experiment[25] show that the wake behind a three-dimensional discrete roughness element is unstable to two families of convective instability modes. One family is the symmetric even modes where the fluctuations associated with the instabilities are symmetric about the symmetry plane. The other family is the anti-symmetric odd modes where the fluctuations associated with the instabilities are 180 degrees out-of-phase about the symmetry plane. For the larger unit Reynolds number case of $Re=10.8*10^6$/m, both experiment and stability calculations for the diamond-shape roughness indicate that one of the even modes, with a peak frequency of ~100 kHz, dominates the transition process in the roughness wake. Of less importance in that case, is an odd-mode instability with a peak frequency of ~50 kHz. To understand how freestream acoustic disturbances generate these instability waves, we superimposed two and three-dimensional acoustic disturbances on the outer part of the computational domain and investigated the generation and evolution of the unsteady disturbances in the roughness wake.

The acoustic field that impinges on the outer boundary is taken to be in the following form.

$$p'_{ac} = \text{Real}\left\{ \tilde{p}_{ac} e^{i\alpha_{ac}x + i\beta_{ac}z - i\omega t} \right\} \tag{7}$$

Here α_{ac}, β_{ac} are the acoustic wavenumbers in the axial and spanwise directions, and ω is the frequency of the acoustic disturbance.

1. Interaction of two-dimensional acoustic disturbances

Two-dimensional slow acoustic disturbances with amplitude of $\tilde{p}_{ac} / p_\infty = 2 * 10^{-5}$ were introduced at the outer boundary of the computational domain and time accurate simulations were performed. The corresponding acoustic mass-flux fluctuations amplitude is $1.02*10^{-5}$. The slow acoustic waves propagate with the phase velocity of (U-c) in the flow direction, where c is the acoustic velocity. We chose the slow acoustic wave because the receptivity at the plate leading edge to slow waves is much larger compared to that for the fast wave. The results are first presented for a frequency of 100 kHz and for the flow over the diamond-shape roughness at the unit Reynolds number of Re = $10.8*10^6$/m. Contours of the computed density fluctuations are shown in Figs. 12(a, b). Figure 12(a) presents the density fluctuations for the computational domain, while Fig. 12(b) presents a close-up view of the density fluctuations in the vicinity of the roughness. The figures show that well organized disturbances approach the roughness element from upstream and transmit through the compression waves unmodulated in amplitude or wavelength. It is also observed that the freestream disturbances do not directly interact with roughness. The wavelength of the disturbances in this case is about 4.8 mm and the width of the roughness in the axial and spanwise directions is 3.6 mm. Figure 13(a) displays contours of mass-flux perturbations in the (x-z) plan view at a constant grid plane of $y/\delta \sim 0.8$ across the middle of the boundary layer. As expected the two-dimensional symmetric freestream disturbances generate disturbances along the symmetry plane, and it is also interesting to observe that the disturbances are confined to a narrow region in the spanwise direction. Figure 13(b) depicts a three-dimensional view of the iso-surfaces of the mass-flux perturbations near the roughness while Fig. 13(c) shows the total mass-flux, i.e., the perturbations and the mean flow, in the region farther downstream, $x \sim$ 140-150 mm, where the disturbances have amplified to finite values. It is seen that the due to the interaction, hairpin-type vortices are shed by the interaction and farther downstream these vortices become stronger and breakdown to turbulence.

Figure 14 presents the evolution of the maximum mass-flux fluctuations along the centerline of the roughness wake. Figure 14(a) displays the results in log-scale and Fig. 14(b) shows the results in linear scale. We also indicate the streamwise location of the roughness elements by a black bar in the figures. The results show that the disturbances along the centerline first decrease past the roughness until x ~ 55 mm and reach the lowest amplitude of $1*10^{-5}$. Beyond this neutral point, the disturbances grow exponentially and saturate around an amplitude of 0.4 near $x \sim$ 160 mm. The fluctuating amplitudes reach about 80 percent of the free stream values. We also included the computed maximum RMS (root mean square) values for the mass fluctuations and compared it with the experimental measurement[25]. The black circles show the measured spectral amplitude at 100 kHz obtained by integrating the spectrum across ±1 kHz. The measured maximum RMS value at x = 84.7 mm is $2.8*10^{-4}$, and the computed value is $9.5*10^{-4}$. The blue circles are the results obtained by multiplying the black circles by the ratio between the measured and computed value (a factor of 3.3). The agreement between the measured and the computed values are very good up to the saturation. This may be due to the fact that in the simulation we introduced only one frequency, while in the experiment, there exists a broadband of frequencies.

Figures 15(a-d) show contour plots of the RMS distribution for the mass-flux fluctuations in the cross sectional (z-y) plane at axial stations of x = 49.97, 76.07, 110.57 and 136.57 mm. We also plotted the mean mass-flux as white line contours in the figures for reference. Note that the maximum contour levels are different in each figure. The first observation is that maximum RMS values of the disturbances are situated in the high wall-normal shear region along the symmetry line (z = 0). We also notice disturbances appear in the spanwise high shear regions as well. The fluctuations in the inner shear region are larger than those in the outer shear region. These results are similar to the shape of the dominant even mode computed using two-dimensional stability analysis[20] and with the experimentally observed contour shapes[25]. Figure 16 shows the RMS mass-flux profiles for a frequency f = 100 kHz at different axial stations along the roughness wake centerline. As we discussed earlier, the peak amplitudes are located in the high shear region in the wake. The maximum amplitude at x = 110.6 mm is about 0.02 and it increases to 0.23 near x = 153.2 mm. The conclusion is that the freestream acoustic disturbances generate the even mode instability with the maximum mass-flux fluctuations equals to the free stream acoustic mass-flux amplitude behind a three-dimensional roughness element.

The experiments performed in the Purdue University BAM6QT tunnel[28] revealed that the transition Reynolds number behind an isolated roughness increased by a factor of 6.4 under quiet-flow conditions compared to noisy conditions. To see what changes occur in the generation and the evolution of disturbances behind the roughness in high-noise conditions, we performed a simulation with a high free stream noise level of $2*10^{-3}$, which is 100 times larger than that was simulated previously. We included the maximum mass-flux fluctuations obtained for this case in Fig. 14(a, b). It is seen that the initial generation and evolution are the same as in the lower amplitude case except that the initial amplitude levels are 100 times larger. The amplitude saturation occurs earlier at about $x \sim 90$ mm compared to $x \sim 150$ mm in the low-amplitude case. This implies that even in noisy conditions, the generation and the evolution of instability waves are still governed by a linear process, and in the high amplitude case, the saturation of amplitude and breakdown to turbulence will occur much earlier.

Figures 17(a, b) show the simulation results for the flow over square-shape roughness. Figure 17(a) depicts the evolution of the maximum mass-flux fluctuations along the centerline of the roughness wake and Fig. 17(b) displays the contours of the RMS mass-flux fluctuations in the cross-sectional (y, z) plane at an axial location of $x = 153$ mm. We also included the results for the diamond box case in Fig. 17(a). The first observation is that the generation and the evolution of the disturbances and the flow features are similar to the flow over the diamond-shape roughness. The amplitude of the fluctuations at the neutral point is about $0.5*10^{-5}$, which is two times smaller than for the diamond-shape roughness. The growth rate is also smaller for this frequency. The amplitude at $x = 140$ mm is about 0.07 in this case compared to 0.35 in the diamond shape roughness case. However, the most amplified frequencies may be different than the 100 kHz we simulated in this case. We have to perform a stability analysis and simulations with a broadband of frequencies to compare the results. The conclusion is that the flow dynamics are the same in both cases. Similarly Figs. 18(a, b) show the results for the flow over the diamond shape roughness at the lower Reynolds number of $Re=9.0*10^{-6}$/m for a frequency of 100 kHz. The amplitude of the fluctuations at the neutral point is $2 * 10^{-6}$ which is five times smaller than that for the higher Reynolds number case. The growth rate is initially the same as that for the higher Reynolds number case, but the growth rate downstream becomes smaller than that for the higher Reynolds number case.

2. Interaction of three-dimensional acoustic disturbances

Similar to the two-dimensional case, three-dimensional slow acoustic disturbances with amplitude of $\tilde{p}_{ac} / p_{\infty} = 1*10^{-5}$ were introduced at the outer boundary of the computational domain and time accurate simulations were performed. The spanwise wavelength of the acoustic disturbances is 1/4th of the width of the roughness $\lambda_{z,ac} = 2.54*\sqrt{2}/4 = 1.27\ mm$. The results are first presented for a frequency of 100 kHz and for the flow over the diamond-shape roughness at the unit Reynolds number of $Re=10.8*10^{6}$/m. Figures 19(a-d) display the contours of mass-flux perturbations in the (x-z) plan view at a constant grid planes J=60 ($y/\delta \sim 0.4$) and 104 ($y/\delta \sim 0.8$) across the boundary layer. Figure 19(a, b) show the results on the J=60 ($y/\delta \sim 0.4$) and J=104 ($y/\delta \sim 0.8$) planes for $30 < x < 90$ mm, and Figs. 19(c, d) display the contours farther downstream $90 < x < 150$ mm across the same J=60 ($y/\delta \sim 0.4$) and 104 ($y/\delta \sim 0.8$) planes. Comparing all four figures, we observe that two kinds of disturbances are generated by the interaction of three-dimensional acoustic disturbances with an isolated three-dimensional roughness. One is confined to the sides of the roughness. They are asymmetric about the symmetry line and they persist for the whole domain from $x \sim 40$ to 150 mm. The second kind is the disturbances that are growing along the symmetry line. These disturbances are small in amplitude up to $x \sim 120$ mm and started to amplify farther downstream.

Figures 20(a-d) show the contour plots of the RMS distribution for the mass-flux fluctuations in the cross sectional (z-y) plane at axial stations $x = 49.97$, 76.07, 110.57 and 136.57 mm. We also included the mean mass-flux as white line contours in the figures for reference. Note that the maximum contour levels are different in each figure. The first observation is that up to $x \sim 110$ mm, the maximum fluctuations are situated in the spanwise high shear layer regions. We also should note that the disturbances are not exactly symmetric about the centerline. This is due to the fact that we imposed only one acoustic wave with a positive β_{ac} in the simulation. We observe maximum disturbances on the side of the roughness at $x \sim 110$ mm compared to that along the centerline. At $x \sim 136$ mm, the maximum RMS of the disturbances appears on the symmetry plane. The amplitudes of the fluctuations in the symmetry plane are larger than that appearing in the outer shear region. The maximum RMS value at the symmetry plane is about 0.006 and along the side it is about 0.004.

Figure 22(a) shows the evolution of the maximum mass-flux fluctuations along the centerline and off the centerline for the frequency of $f = 100$ kHz. There are four curves in the plot. The red line is the growth of the maximum fluctuations along the centerline. The blue line is the maximum in the region $z > 0.8$ mm, the green line is the maximum in the region $z > 0.4$ mm, and the black line is the maximum in the whole region, $z > 0.0$.

The figure shows that up to $x \sim 117$ mm, the fluctuations consist of two different modes. One is the black and blue line that represent the odd or the asymmetric mode located on the side of the roughness as observed in Figs. (19) and (20). The other is the red line that represents the even mode that grows along the centerline. In the earlier computations[20, 21], they also predicted two kinds of instability modes. One is the even mode and the other is odd mode. The simulation results agree with this prediction. The odd mode started to grow from $x \sim 60$ mm and the even mode started to grow from $x \sim 85$ mm. The growth of the even mode is stronger than the odd mode. The amplitude of the even mode and the odd modes become equal around $x \sim 117$ mm. It is interesting to note that the odd mode persists only up to $x \sim 125$ mm, and beyond that the odd mode ceases to appear separately — only the symmetric mode exists. At this point we do not know why or how the odd mode merged with the even mode. This needs further investigation. Figures 21(a-d) and 22(b) similarly depict the results for a frequency of $f = 50$ kHz. The amplitude along the centerline remains the highest up to $x \sim 100$ mm. Between $100 < x < 135$ mm, the amplitude off the centerline $z > 0.404$ mm becomes the highest, beyond that the amplitude along the centerline becomes the highest again. It appears that both modes, the even and the odd modes, are excited by the three-dimensional acoustic disturbances. A modal analysis, not yet performed, would be needed to separate these modes.

V. Conclusions

The interaction of two and three-dimensional free stream acoustic disturbances with a discrete three-dimensional roughness is numerically investigated in a supersonic boundary layer. A diamond-shape and a square-shape roughness are simulated at two units Reynolds numbers. The results showed that the wake behind the roughness consists of two counter-rotating vortices on either side of the roughness. These vortices lift the low momentum fluid towards the outer layer and high momentum fluids towards the wall. This manifests into long low-speed and high-speed streaks behind the roughness. These are in qualitative and quantitative agreement with the previous computations[20,21] and experiment[25].

The simulations of the interaction of two-dimensional acoustic disturbances with diamond and square shape roughness elements revealed that the disturbances behind the roughness first decays for up to 50 roughness heights and then increases exponentially downstream before saturating at finite amplitudes. These simulations, and the previous stability computations[20] and the experiment[25], conclude that two-dimensional freestream disturbances generate the even mode instability downstream of the roughness wake. The maximum mass-flux fluctuation amplitude is equal to the amplitude of the free-stream acoustic mass-flux fluctuations levels. The computations performed at very high acoustic levels revealed that even under noisy conditions the generation and the evolution of disturbances behind the roughness is still governed by the linear process.

The simulations of the interaction of three-dimensional acoustic disturbances with a diamond shape roughness element revealed that both even and odd instability modes are generated in the roughness wake. The initial amplitudes of the mass-flux fluctuations for these modes are about 3.5 times the amplitude of the free stream acoustic mass-flux fluctuations amplitude. The odd mode started to grow from farther upstream compared to the even mode. However, the odd mode grows slowly compared to the even mode and the amplitudes of the odd and even mode become equal in downstream. Farther downstream of this region, the even mode overtakes the odd mode and dominates the flow field.

References

[1]Mack, L., "Boundary Layer Stability Theory," JPL Report No. 900-277 Rev. A, Pasadena, Calif, Nov. 1969.

[2]Goldstein, M. E., "The Evolution of Tollmien-Schlichting Waves near a Leading Edge," *J. Fluid Mech*. (1983), 127:59-81.

[3]Goldstein, M. E., "Scattering of Acoustic Waves into Tollmein-Schlichting Waves by Small Streamwise Variation in Surface Geometry," *J. Fluid Mech*., (1985), 154:509-29.

[4]Fedorov, A. V., "Transition and Stability of High-Speed Boundary Layers," *Annu. Rev. Fluid Mechanics*, 2011. 43:79-95.

[5]Balakumar, P., "Receptivity of a Supersonic Boundary Layer to Acoustic Disturbances," *AIAA Journal*, Vol. 47, No. 5, May 2009, pp. 1034-1041

[6]Ma, Y. and Zhong, X., "Receptivity of a Supersonic Boundary Layer over a Flat Plate. Part 2. Receptivity to Freestream Sound," *J. Fluid Mech.*, Vol. 488, 2003, pp. 79-121.

[7]Balakumar, P., and Kegerise, M. A., "Receptivity of Hypersonic Boundary Layers to Acoustic and Vortical Disturbances," AIAA Paper 2011-0371, January 2011.

[8]Balakumar, P., "Receptivity of Hypersonic Boundary Layers to Distributed Roughness and Acoustic Disturbances", 50th AIAA Aerosciences Meeting, Dallas, TX, January 7-10, 2013.

[9]Klebanoff, P. S., and Tidstrom, K. D., "Mechanisms by which a Two-Dimensional Roughness Element Induces Boundary Layer Transition," *Phys. Fluids* 15, 1972, pp. 1173-1188.

[10]Klebanoff, P. S., Cleveland, W. G., and Tidstrom, K. D., "On the Evolution of a Turbulent Boundary layer Induced by a Three-dimensional Roughness Element," *J. Fluid Mech*. (1992), vol. 237, pp. 101-187.

[11]Acarlar, M. S., and Smith, C. R., "A Study of Hairpin Vortices in a Laminar Boundary Layer. Part 1. Hairpin Vortices Generated by a Hemisphere Protuberance," *J. Fluid Mech*. (1987), vol. 175, pp. 1-41.

[12]Gregory, N., and Walker, W. S., "The Effect on Transition of Isolated Surface Excrescences in the Boundary layer," Aero. Res. Counc. R. & M. 2799, 1956.

[13]Reda, D. C., "Review and Synthesis of Roughness-Dominated Transition Correlations for Reentry Applications," *J. Spacecraft and Rockets* 39 2, 2002, pp. 161-167.

[14]Schneider, S. P., "Summary of Hypersonic Boundary-Layer Transition Experiments on Blunt Bodies with Roughness," *J. Spacecraft and Rockets* (2008), 45 6:1090-1105.

[15]Schneider, S. P., "Flight Data for Boundary-Layer Transition at Hypersonic and Supersonic Speeds," *J. Spacecraft and Rockets*, 36 1, 1999, pp. 8-20.

[16]Berry, S. A., and Hovarth, T. J., "Discrete-roughness Transition for Hypersonic Flight Vehicles," *J. Spacecraft and Rockets*, Vol. 45, No.2 2008, pp. 216-227.

[17]Danehy, P.M., Bathel, M., Ivey, C., Inman, J. A., and Jones, S. B., "NO PLIF Study of Hypersonic Transition over a Discrete Hemispherical Roughness Element," AIAA Paper 2009-394, January 2009.

[18]Wheaton, B. and Schneider, S., "Roughness-Induced Instability in a Laminar Boundary Layer at Mach 6," AIAA Paper 2010-1574, 2010.

[19]Bartkowicz, M., Subbareddy, P. K., and Candler, G., "Numerical Simulation of Roughness Induced Instability in the Purdue Mach 6 Wind Tunnel," AIAA Paper 2010-4723, 2010.

[20]Choudhari, M., Li, F., Wu, M., Chang, C., Edwards, J., Kegerise, M., and King, R., "Laminar-Turbulent Transition behind Discrete Roughness Elements in a High-Speed Boundary Layer," AIAA Paper 2010-1575, January 2010.

[21]Choudhari, M., Li, F., Chang, C., Norris, A., Edwards, J., "Wake Instabilities behind Discrete Roughness Elements in High Speed Boundary Layers," AIAA Paper 2013-0081, January 2013.

[22]Chang, C.-L., Choudhari, M., and Li, F., "Numerical Computations of Hypersonic Boundary-Layer over Surface Irregularities," AIAA Paper 2010-1572, 2010.

[23]Iyer, P. S., Muppidi, S., and Mahesh, K., "Roughness-induced transition in high speed flows," AIAA Paper 2011-566, January 2011.

[24]Marxen, O., Iccarino, G., and Shaqfeh, S. G., "Numerical Simulations of hypersonic boundary-layer instability with localized roughness," AIAA Paper 2011-567, January 2011.

[25]Kegerise, M., King. R., Owens, L. Choudhari, M., Norris, A., Li, F., and Chang, C. L., "An Experimental and Numerical Study of Roughness-Induced Instabilities in a Mach 3.5 Boundary Layer," AVT-Specialists Meeting on Hypersonic Laminar-Turbulent Transition, April 16-19, 2012, San Diego, CA.

[26]Shu, C.W., "Essentially Non-Oscillatory And Weighted Essentially Non-Oscillatory Schemes For Hyperbolic Conservation Laws," NASA/CR-97-206253 and ICASE Report No. 97-6.

[27]Atkins, H.L., "High-Order ENO Methods for the Unsteady Compressible Navier-Stokes Equations," AIAA Paper 91-1557, 1991.

[28]Casper, K., Wheaton, B., Johnson, H., and Schneider, S., "Effect of Freestream Noise on Roughness-Induced Transition at Mach 6," AIAA Paper 2008-4291, 2008.

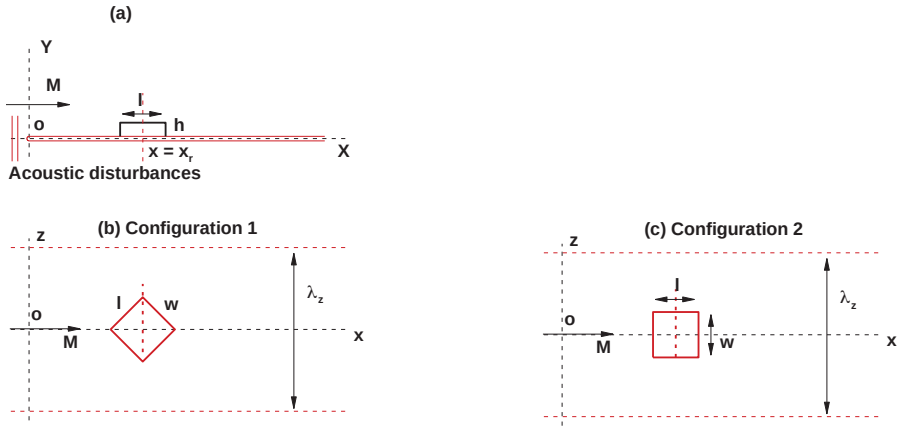

Figure 1. Schematic diagrams of the roughness configurations placed on a flat plate. (a) Flat plate and roughness in the (x-y) plane, (b) roughness configuration 1 in the plan view (x-z) plane, and (c) roughness configuration 2 in the plan view in the (x-z) plane.

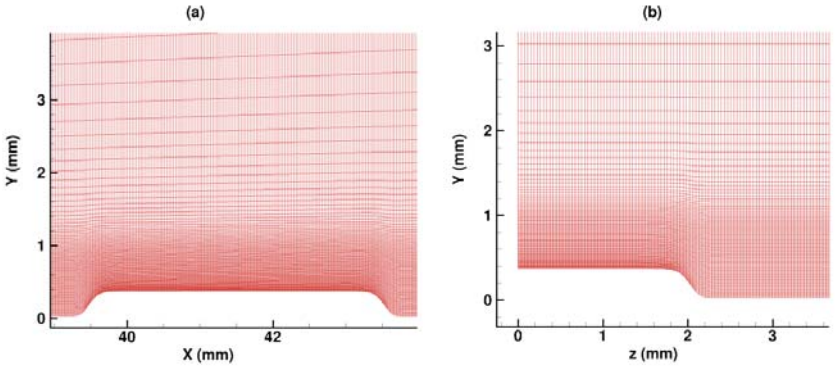

Figure 2. Grid distributions over the roughness element: (a) in the axial (x-y) plane, and (b) in the spanwise (y-z) plane.

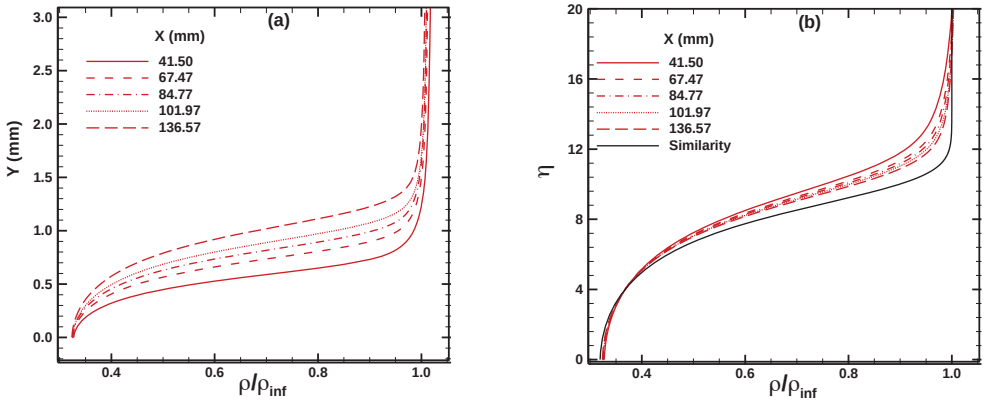

Figure 3. Smooth wall boundary layer density profiles at different axial locations for a unit Reynolds number of $10.8*10^6$/m: (a) the height in mm and (b) the height in similarity coordinate.

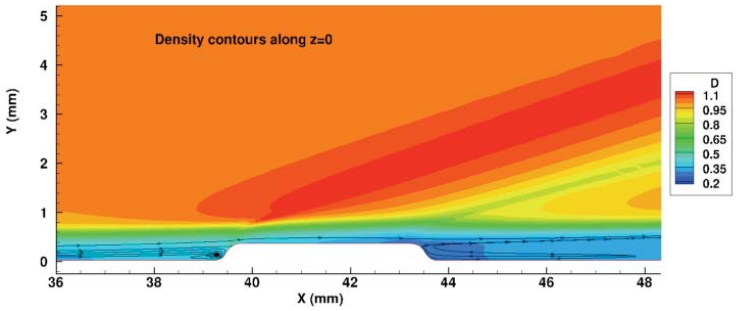

Figure 4. Density contours over the roughness in the (x-y) plane at z=0.

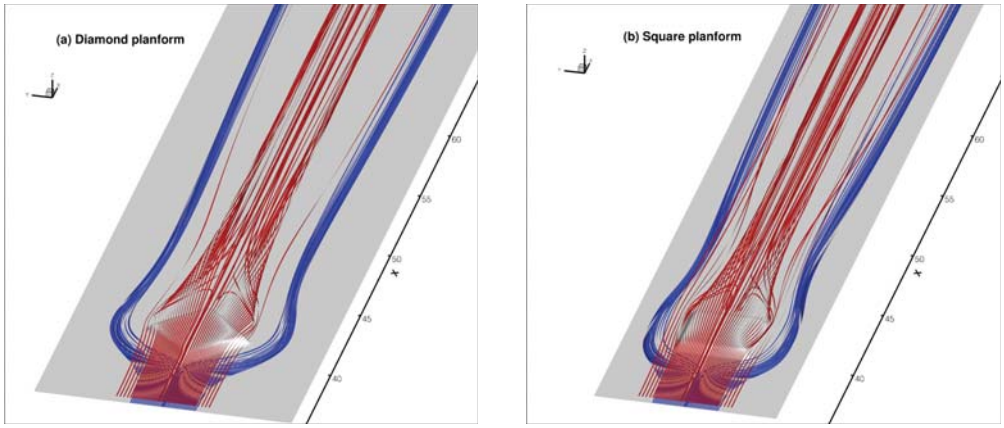

Figure 5. Streamlines over the roughness (a) diamond shape, (b) square shape. The blue streamlines originate from a height of y/δ~0.45 and the red streamlines originate from y/δ~0.7.

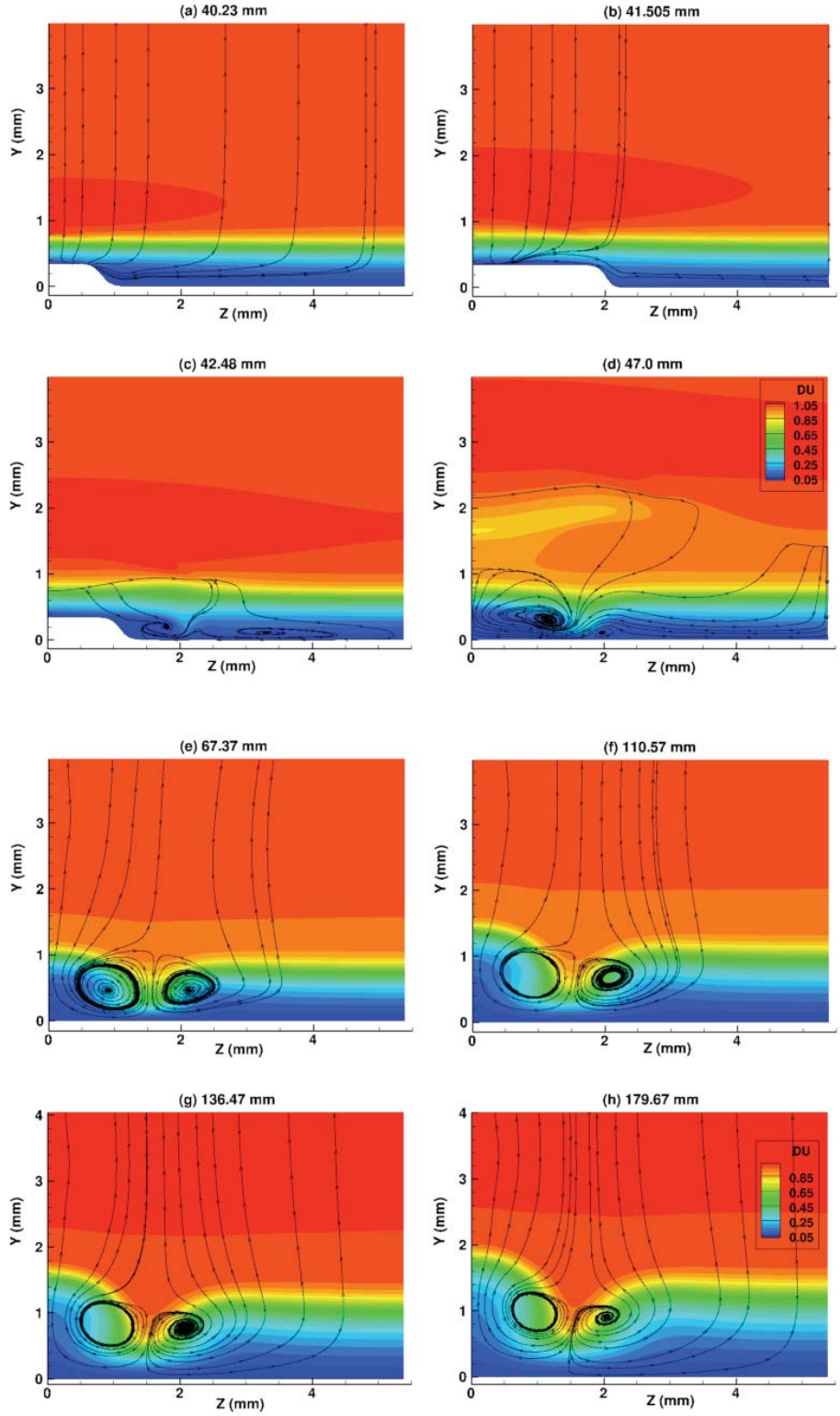

Figure 6. Mass flux contours and the streamlines in different cross sectional (z-y) planes at increasing x stations.

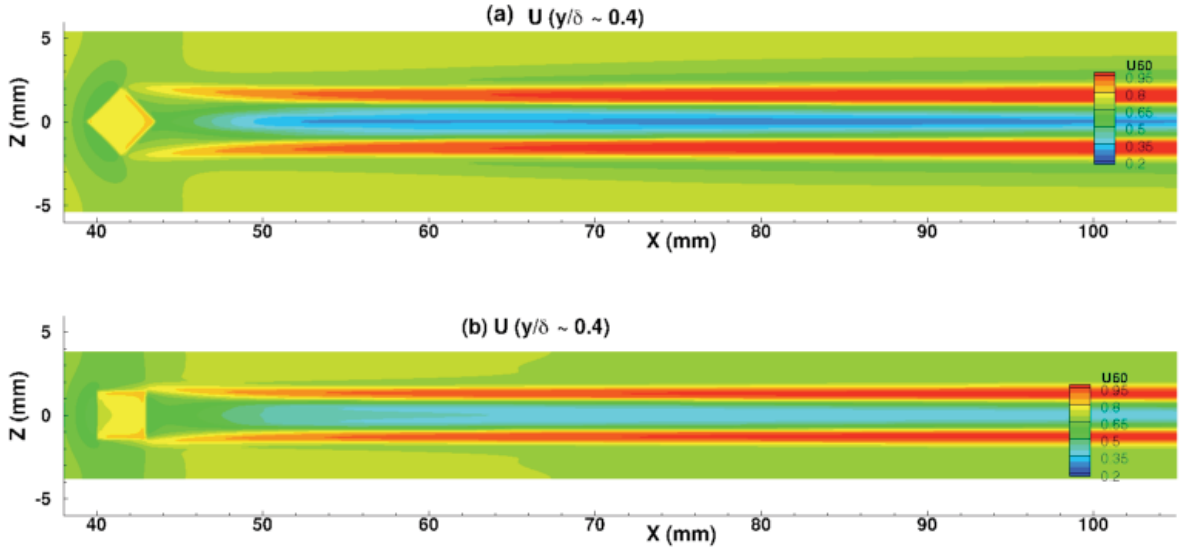

Figure 7. Streamwise velocity contours in (x-z) plane across the middle of the boundary layer, y/δ ~ 0.4. (a) Diamond shape, (b) square shape.

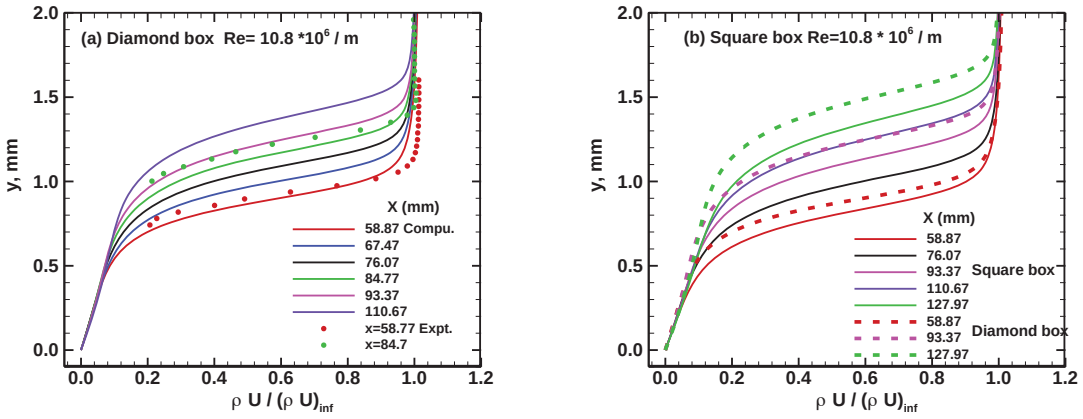

Figure 8. Computed and measured boundary layer mass-flux profiles at different axial locations with roughness (a) diamond shape, (b) square shape.

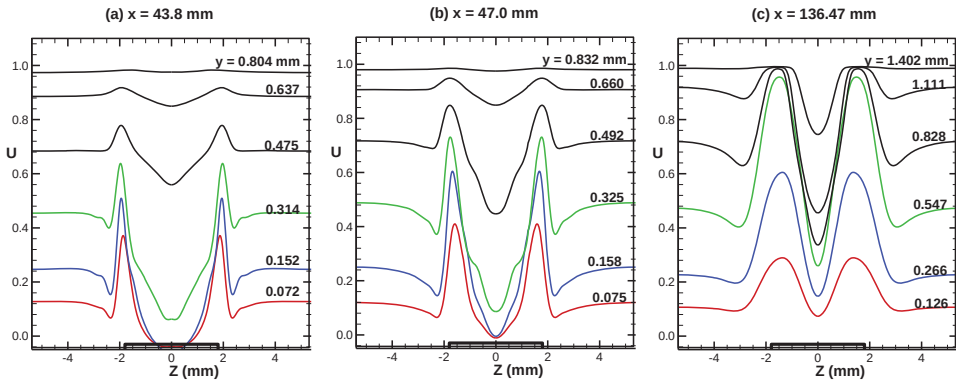

Figure 9. Streamwise velocity variation in the spanwise direction at different boundary layer heights for the diamond-shape roughness.

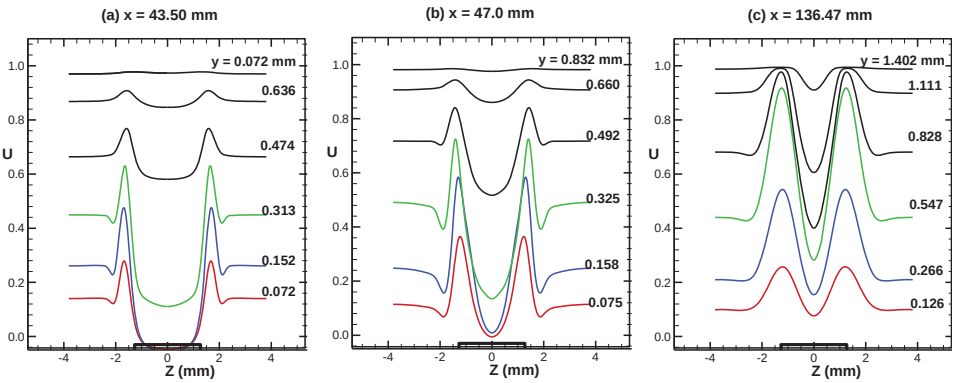

Figure 10. Streamwise velocity variation in the spanwise direction at different boundary layer heights (Square shape).

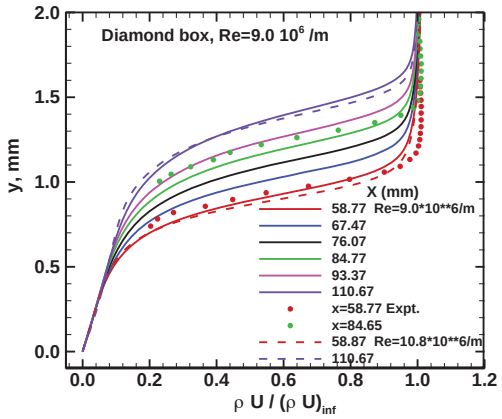

Figure 11. Computed and measured mass-flux profiles on the roughness wake symmetry plane at different axial locations (diamond-shape roughness with unit Reynolds number of Re = 9.0*10^6/m).

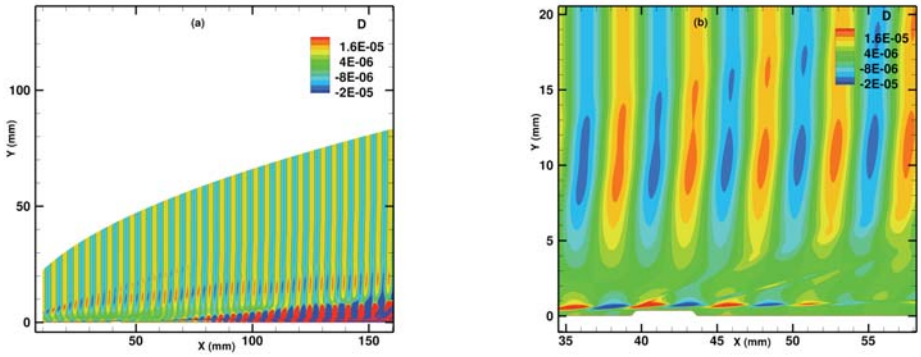

Figure 12. Density fluctuations in the symmetry plane (z = 0) generated by the interaction of a slow acoustic wave with an isolated diamond shape roughness: (a) computational domain and (b) in the vicinity of the roughness. f = 100 kHz, Re = 10.8*10^6/m.

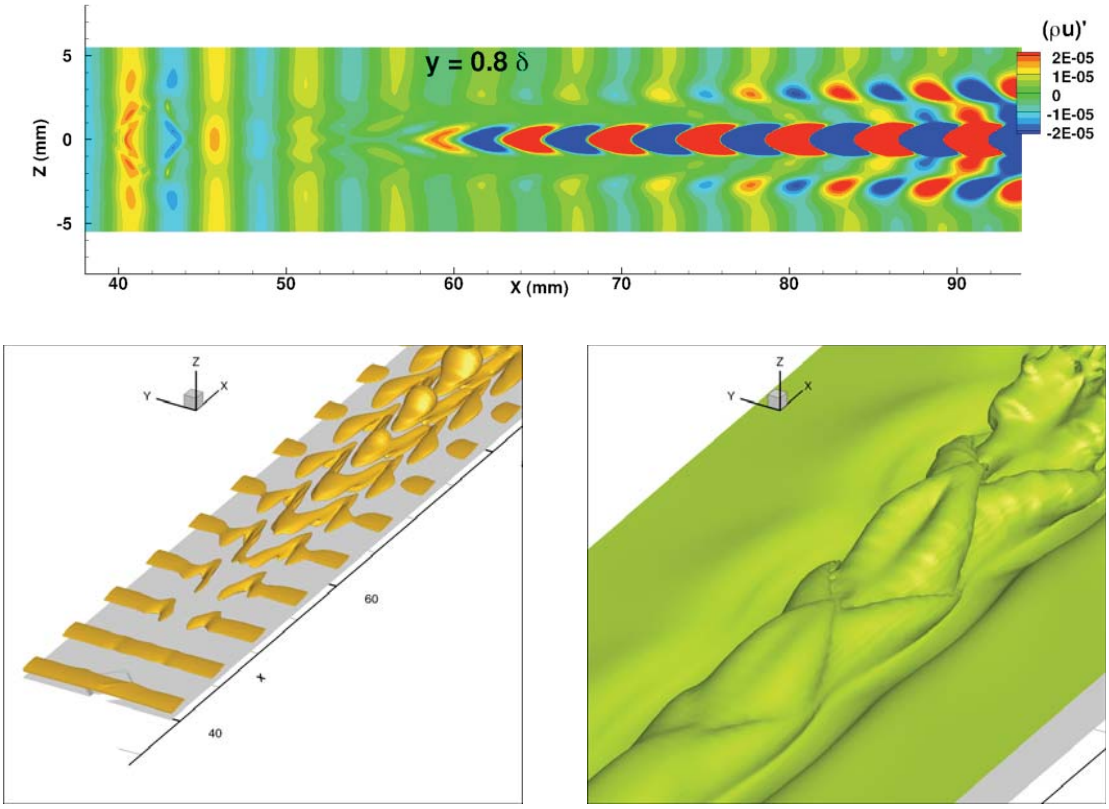

Figure 13. (a) Mass-flux fluctuations in (x-z) plane across the middle of the boundary layer (b) mass-flux fluctuation iso-surface in a three-dimensional view close to the roughness, (c) total mass-flux three-dimensional view, generated by the interaction of a slow acoustic wave with an isolated diamond shape roughness. f = 100 kHz, Re = 10.8*10^6/m.

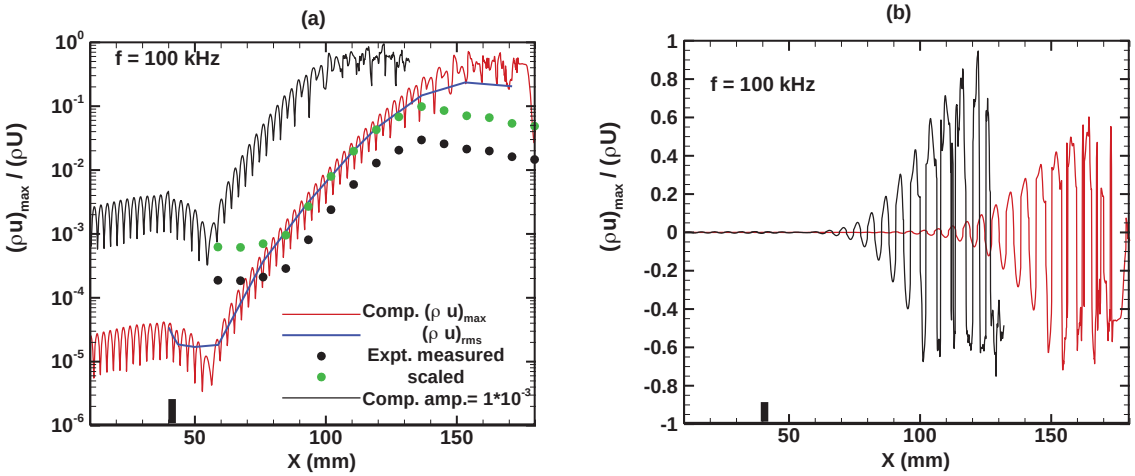

Figure 14. Growth of the maximum mass-flux fluctuations along the centerline of the diamond shape roughness: (a) in log-scale and (b) in linear scale. Re=10.4*10^6/m, f=100 kHz

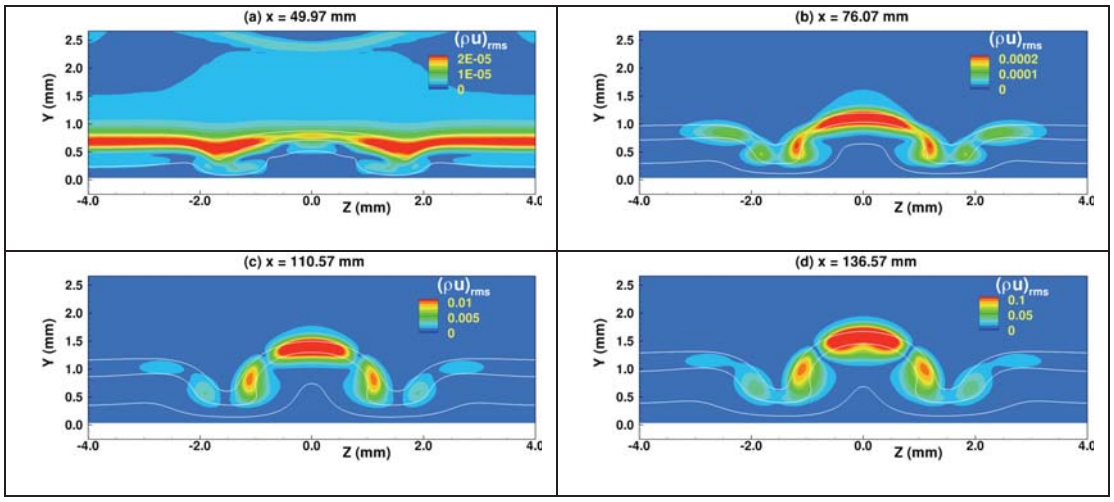

Figure 15. Contours of the RMS of the mass-flux fluctuations in the cross sectional plane at different axial stations.

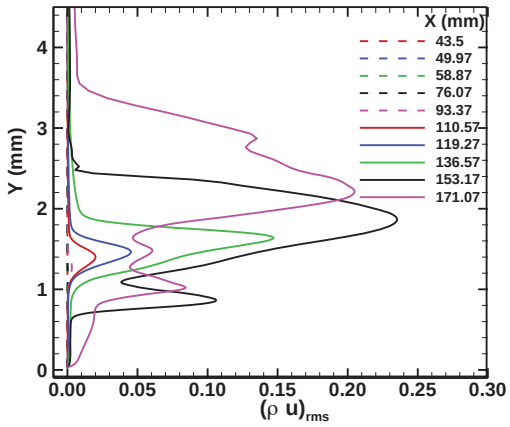

Figure 16. Boundary layer RMS profiles of the mass-flux fluctuations at different axial locations f=100 kHz.

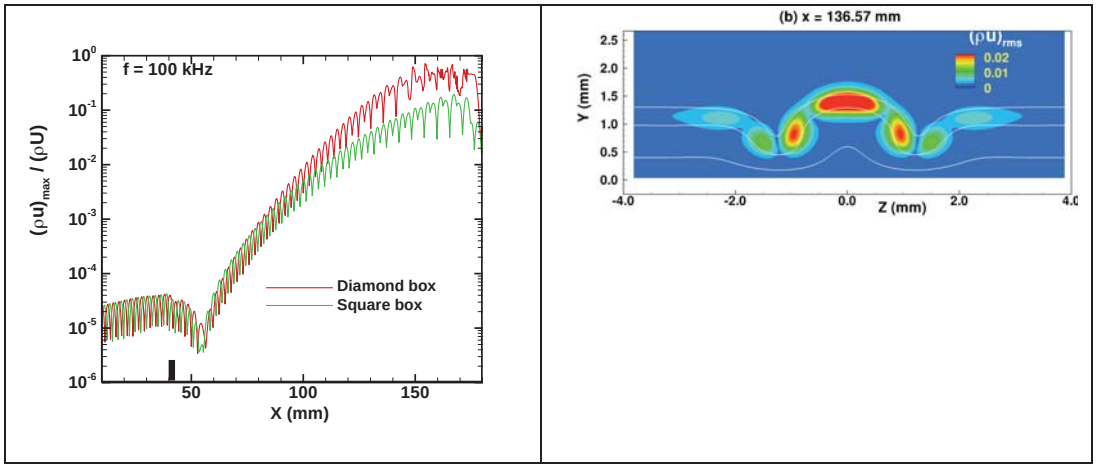

Figure 17. (a) Growth of the maximum mass-flux fluctuations along the centerline of the square shape roughness, (b) contours of the RMS at an axial location x=136.57 mm. Re=10.8*10^6/m, f=100 kHz.

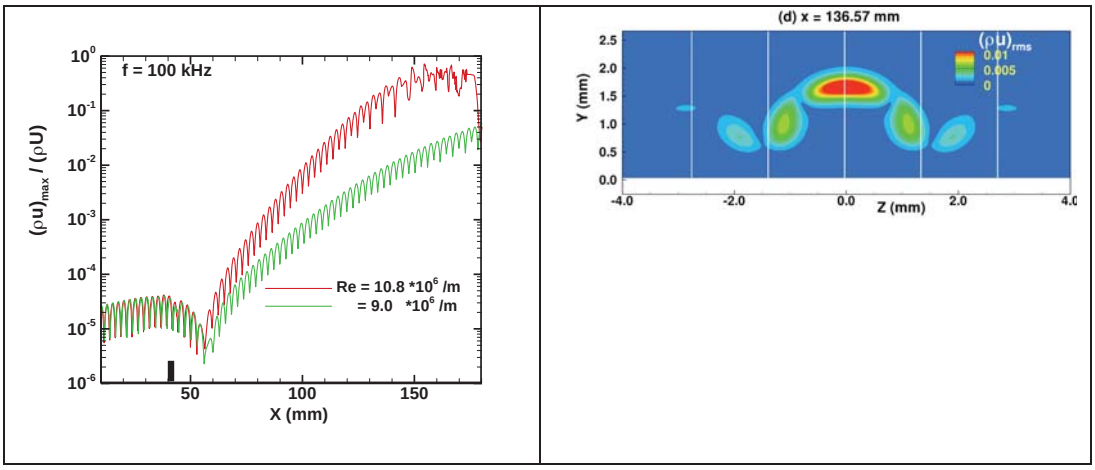

Figure 18. (a) Growth of the maximum mass-flux fluctuations along the centerline of the diamond shape roughness, (b) contours of the RMS at an axial location x=136.57 mm. Re=9*10^6/m, f=100 kHz

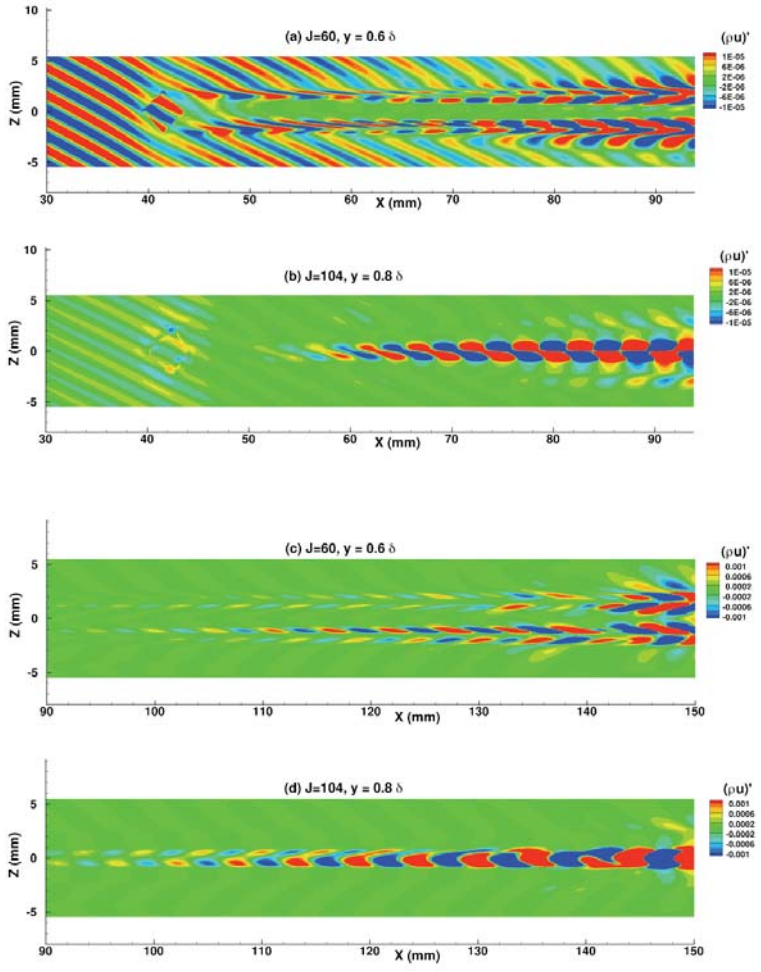

Figure 19. Mass-flux fluctuations in (x-z) plane across different heights in the boundary layer generated by the interaction of a slow three-dimensional acoustic wave with an isolated diamond shape roughness, f=100 kHz, $\lambda_{z,ac}$ = 0.25 b. (a) y/δ=0.6, (b) y/δ=0.8 for x=30-90 mm, (c) y/δ=0.6, and (d) y/δ=0.8 for *x*=90-150 mm.

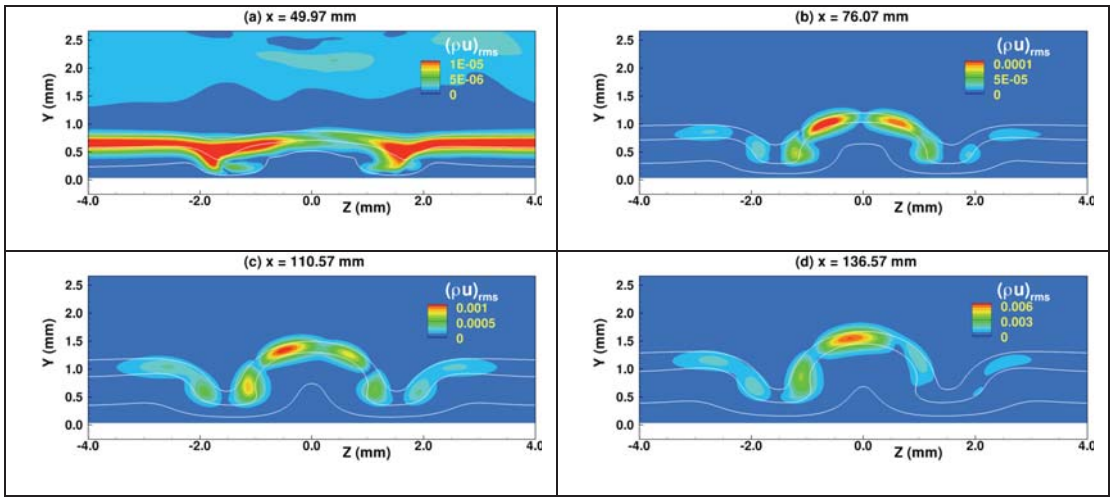

Figure 20. Contours of the RMS of the mass-flux fluctuations in the cross sectional plane at different axial stations generated by a three-dimensional acoustic disturbances, f=100 kHz.

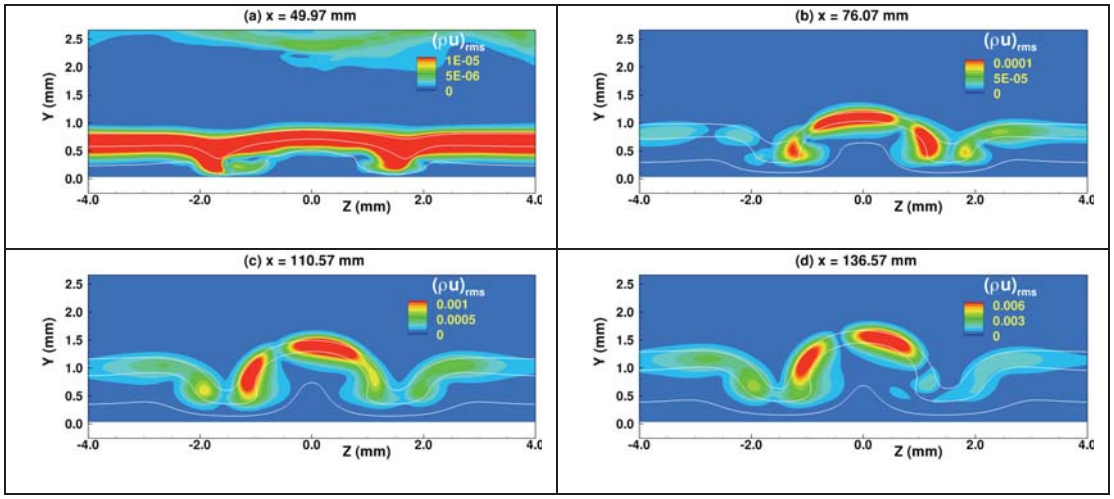

Figure 21. Contours of the RMS of the mass-flux fluctuations in the cross sectional plane at different axial stations generated by a three-dimensional acoustic disturbances, f=50 kHz.

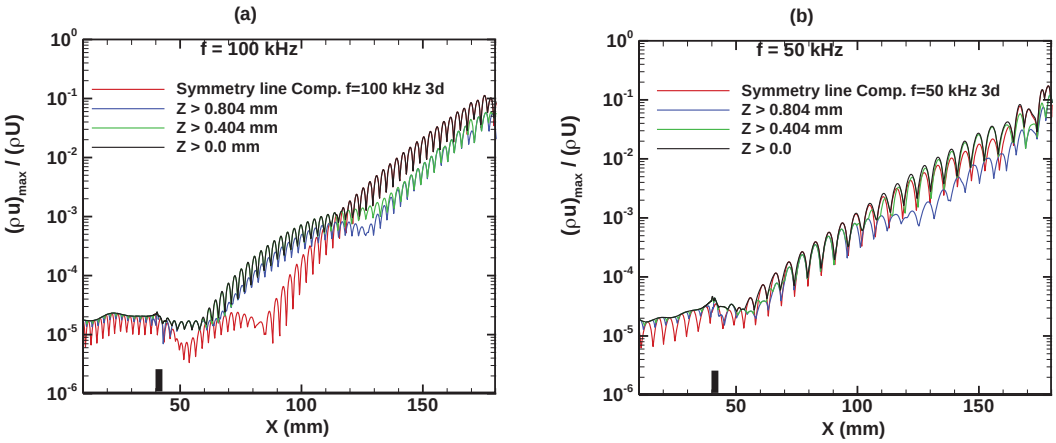

Figure 22.Maximum mass-flux fluctuations generated by a three-dimensional acoustic disturbances along the symmetry line and off the centerline.